communications materials

Article

https://doi.org/10.1038/s43246-024-00506-3

Superlattice assembly strategy of small noble metal nanoparticles for surface-enhanced Raman scattering

Check for updates

Chang Yao[1,2,5], Wuwen Yan[1,2,5], Ronglu Dong[2,3], Shaobin Dou[2,4] & Liangbao Yang[1,2,3]

The self-assembly of noble metal nanoparticles into periodic structures has been a theme of great interest for surface-enhanced Raman scattering (SERS) and use in functional devices. However, small nanoparticle self-assembly faces numerous challenges in tunability, referring to controlling their structural properties like structure, gaps, and arrangement. These issues highlight the need for further research and development to enhance the tunability and stability of self-assembled small nanoparticles. Here, we report a general centimeter-scale superlattice assembly strategy for noble metal nanoparticles less than 15 nm in size. Not only is this monolayer superlattice assembly generally applicable to different kinds and sizes of noble metal nanoparticles, but also, the crystal plane spacing can also be quickly and conveniently controlled by changing the ethanol concentration. SERS results reveal that optimized superlattice membranes of noble metal nanoparticles possess high detection sensitivity and ordered hot spots. Therefore, our strategy offers prospects for high-performance SERS substrates based on small noble metal nanoparticle superlattices.

The self-assembly of noble metal nanoparticles is a process that involves the spontaneous organization of these particles into ordered structures without external intervention. Over the past few decades, surface-enhanced Raman scattering (SERS)[1,2] has attracted much attention due to its great potential for ultrasensitive detection and has quickly emerged as a powerful analytical technique for detection and identification[3–10]. Thus, the self-assembly of noble metal nanoparticles has been extensively studied due to their highly sensitive detection in SERS[11–13]. In recent years, many studies have used self-assembly of nanoparticles (such as nanocubes[14] and nanorods[15]) to create nanofeatured plasmonic substrates that could generate regions of strongly enhanced electromagnetic fields, known as hotspots. it occur at the nanoscale gaps between noble metal nanoparticles, where the electromagnetic field is significantly enhanced due to localized surface plasmon resonance (LSPR) effects[16]. The critical dimensions of interparticle spacings in aggregates are typically in the range of a few nanometers, with smaller gaps leading to stronger electromagnetic field enhancement and higher SERS signal intensity and the enhancement factor of the Raman intensity for molecules near hotspots can often exceed 10^6, resulting in giant amplification[17,18]. However, quantitative SERS analysis in practical applications has been a major problem because of the random and disordered distribution of hotspots on a SERS substrate. Therefore, periodic self-assembly for realizing SERS substrates has been a theme that has attracted much attention[19,20]. periodic self-assembly plays a key role in systematically controlling these critical dimensions by enabling the precise arrangement of nanoparticles into ordered structures with uniform interparticle spacings, thereby optimizing and homogenizing the formation of hotspots. This process is largely driven by van der Waals attraction and ligand repulsion, resulting in stable packed structure with uniform interparticle spacings. In addition, according to previous electromagnetic field simulation results[21,22], for gold nanoparticles (AuNPs), the enhancement factor first increases with increasing particle size, reaches a maximum value at approximately 55 nm, and then decreases with increasing particle size[23–25]. Thus, small noble metal particles, which are often applied to catalysis, have not been widely studied for SERS[26,27].

A nanoparticle superlattice is a periodic array of nanoscale building blocks that can exhibit enhanced optical, electronic, etc. properties[28]. Over the past decade, superlattice self-assembly has been carried out by different methods, and some studies have reported that attaching biomolecules such as DNA, polymers and antibodies to nanoparticle surfaces offers a route to control their superlattice assembly[29–31]. In addition, there are some non-biological molecular assembly methods, such as adjusting the proportion of organic solution to assemble the superlattice[32]. Electrostatic self-assembly

[1]University of Science and Technology of China, Hefei 230026 Anhui, China. [2]Institute of Health and Medical Technology, Hefei Institutes of Physical Science, Chinese Academy of Sciences, Hefei 230031, China. [3]Department of Pharmacy, Hefei Cancer Hospital, Chinese Academy of Sciences, Hefei 230031 Anhui, China. [4]Anhui Cas-art Technology Co. Ltd, Heifei 230088, China. [5]These authors contributed equally: Chang Yao, Wuwen Yan. e-mail: lbyang@iim.ac.cn

forms large 3D crystals by combining different types of countercharged, nearly identical size metal nanoparticles with other types (magnetic or photoluminescent) of nanoparticles[33]. Liquid–air interfacial assembly is a good method for fabricating binary nanocrystal superlattice films, which can be used to create multicomponent nanocrystals for magnetic nanocrystal-based devices[34]. Generally, most of the adjustment of the superlattice plane spacing depends on ligand exchange, which may lead to excessively long adjustment times and the presence of residual molecules, and this method makes the preparation of SERS substrates complex and the substrates less sensitive. Additionally, due to the weak enhancement of the electromagnetic field by traditional small noble metal nanoparticles, there has been limited research on the application of small noble metal nanoparticles in SERS.

In this paper, we constructed a general monolayer superlattice film that can be applied to multiple sizes and categories of noble metal nanoparticles including AuNPs, AgNPs and Au@Ag NPs (in this study, Au@Ag NPs refers to core-shell nanoparticles with gold as the core and silver as the shell, with an overall diameter of approximately 15 nm) to achieve commonality and versatility of SERS. Beyond this, we also designed a brief and effective secondary transfer method that makes the crystal spacing tunable via contraction of ligands of nanoparticles in polar solutions to achieve the best state of the SERS substrate. We utilized grazing-incidence small-angle X-ray scattering (GISAXS), dark-field microscopy, and atomic force microscopy (AFM) to track the entire assembly process. Additionally, we simulated and analyzed the potential energy changes of nanoparticles during the formation of superlattices. Compared with the disorder films of SERS detection using small noble metal nanoparticles, the detection limit is decreased by 1-2 orders of magnitude, and an ordered monolayer nanoparticle superlattice with high-density and uniformly distributed hotspots is obtained. This opens up a new general method for SERS using small nanoparticles that could be applied to different sizes and types, and the method shows promise for further application because of the high sensitivity, high repeatability and high uniformity.

Results and discussions

Construction and assembly process of a monolayer ~13 nm AuNP superlattice

We constructed a monolayer noble metal nanoparticle film via a liquid–air interface to acquire a large-scale long-range-ordered film. Figure 1a shows a diagram of the whole growth process of the monolayer superlattice (the experimental flow chart of the superlattice assembly of AuNPs is shown in Supplementary Fig. 1, and this process is introduced in detail in Supplementary Note I). Figure $1b_{1\text{-}3}$ shows scanning electron microscopy (SEM) images of three superlattice growth stages after the formation of isolated rings, and we also recorded the whole process of monolayer superlattice film formation in situ by dark-field reflection microscopy (Supplementary Fig. 2). First, the nanoparticles present a dispersed state in toluene when injected at the diethylene glycol (DEG) interface, and the nanoparticles rapidly form numerous isolated circular rings to minimize the surface energy of the small particles (Fig. 1a and Supplementary Fig. $2a_3$). Parts of this process may be attributed to the formation of an emulsion due to the residual small amount of water in the nanoparticles during the phase transition[35]. Then, due to toluene evaporation, these isolated rings gradually aggregate through the Marangoni effect[36] (Fig. $1b_1$, Supplementary Fig. $2b_3$), and these processes take only approximately 1 minute.

From 1 to 60 min, these aggregated rings gradually form a lamellar instability quasicrystal lattice (Fig. 1a, b_2), exhibiting several nanoscale plates with lengths ranging from 1 to 2 μm, which are interconnected. The red dashed lines in Fig. $1b_2$ represent the grain boundaries of the nanoscale plates and display Moiré fringes with different orientations[37]. From 60 to 180 min, the grain boundaries in the superlattice disappear, resulting in a large-area, long-range-ordered monolayer film, as shown in Fig. $1b_3$, under the driving force of toluene evaporation for a long time. Additionally, dark-field images (Supplementary Fig. $2c_3$, d_3) reveal that the film interior becomes darker after the formation of the superlattice, indicating an improvement in the crystallinity[38]. From the initial colloidal to final superlattice state, the maximum UV peak of the AuNP film shifts from 527 to 623 nm, and the gradual redshift of the peak indicates a reduction in the nanoparticle gap (Supplementary Fig. $12a_{1\text{-}2}$)[39].

In-plane structure analysis

Then, we discuss the in-plane structure analysis by GISAXS following the AuNP self-assembly process. GISAXS patterns and 1D scattering profiles of different stages were recorded (Fig. $1c_1$–c_3, d_1–d_3), and three representative scattering patterns were taken at 1, 60, and 180 min to determine $q_{||}$ (the in-plane scattering vector in the context of GISAXS analysis). In the initial stage, there is only a weak scattering signal near the beam stop (Fig. $1c_1$, d_1), which implies that the aggregated rings do not form an ordered structure (Fig. $1b_1$). After 60 min, diffraction rods appear in the GISAXS pattern (Fig. $1c_2$, d_2). Fig. $1c_2$ shows that the main scattering peak starts to appear, and X-ray diffraction peaks appear at $q_{||}$ values of ±0.038, ±0.067, ±0.076, and ±0.099 $Å^{-1}$ which can be calculated in Fig. $1d_2$. However, the full width at half maximum (FWHM) is wide, indicating poor crystallinity of the superlattice; at this time, many quasicrystalline islands are spliced together. After long-term continuous growth, the area is fully occupied by the AuNPs, and a stable 2D hexagonal close-packed (hcp) monolayer is formed, whose X-ray diffraction peaks show $q_{||}$values of ±0.039, ±0.069, ±0.079, and ±0.0108 $Å^{-1}$ at 180 min (Fig. $1c_3$, d_3, Supplementary Fig. 3c), which have shifted toward the high region, indicating a smaller crystal plane spacing. Then, according to the formula gap = $2\pi/q - D$ (where q is the scattering vector and D is the diameter of AuNPs), the gap between two nanoparticles from formation to the final state is calculated to be ~3.6 nm and ~3.1 nm. This implies that oleylamine (OAM) is prone to deform and wind up, resulting in significant crossing between molecules from neighboring particles[40] in the low-density surface coverage state and thus in an interparticle spacing of less than two molecular lengths, which is ~4 nm. Additionally, the superlattice structure tends to be stable due to the gradual trapping of nanoparticles into potential wells (the specific details will be discussed below: Interaction potential in superlattice formation). Based on the Lorentz correction of Supplementary Fig. 3a–c, the shape of the final stage peak becomes sharper, and the FWHM narrows, indicating the formation of a more pronounced periodic structure. In addition, according to the out-of-plane structure analysis in Supplementary Fig. 4, there are obvious flat parts of the oscillation peaks and valleys in the 1D scattering curves of q_z (the out-of-plane scattering vector in the context of GISAXS analysis) as time increases, indicating the gradual formation of a superlattice and a nanoparticle transition from dispersion to aggregation. The characteristic oscillation peaks of spherical particles are masked by the structural signals between particles, which is in agreement with the integrated curve in the $q_{||}$ direction. For X-ray scattering from a 2D superlattice structure (Fig. $1c_{1\text{-}3}$, $d_{1\text{-}3}$), we assign Miller indices of $\{hk\}$ to the peaks measured for the Au monolayer. The calculation assumes a hexagonal lattice, where a and b are the bases of the unit cell, and α is the angle between a and b. In other words, the 2D hexagonal lattice has $a = b$ and α = 120°. The line is taken along the $q_{||}$ direction around 0.039 $Å^{-1}$, where the scattering is most intense (marked with red bars; others are marked with green bars in Fig. 1d). The ratios of the Bragg diffraction peak positions are $q\{hk\}/q\{10\} \approx 1 : \sqrt{3} : \sqrt{4} : \sqrt{7} : \sqrt{9}$, which is consistent with a 2D hexagonal structure. The Miller indices of the corresponding superlattice facets are $\{1,0\}$, $\{\bar{1}1\}$, $\{20\}$, and $\{2\bar{1}\}$.

Interaction potential in superlattice formation

The long-term stability of the monolayer superlattice and its interplanar spacing in the unit cell have been interesting issues[41,42]. Therefore, we delved deeper into this topic by exploring the interaction potential of the superlattice for AuNPs and calculating the centroid distance and interparticle potential energy for AuNPs as a function of time (the detailed model construction and interaction are described in Supplementary Note II, including Supplementary Fig. 5). We performed molecular dynamics calculations based on the NVT ensemble of GROMACS to obtain the distribution of the

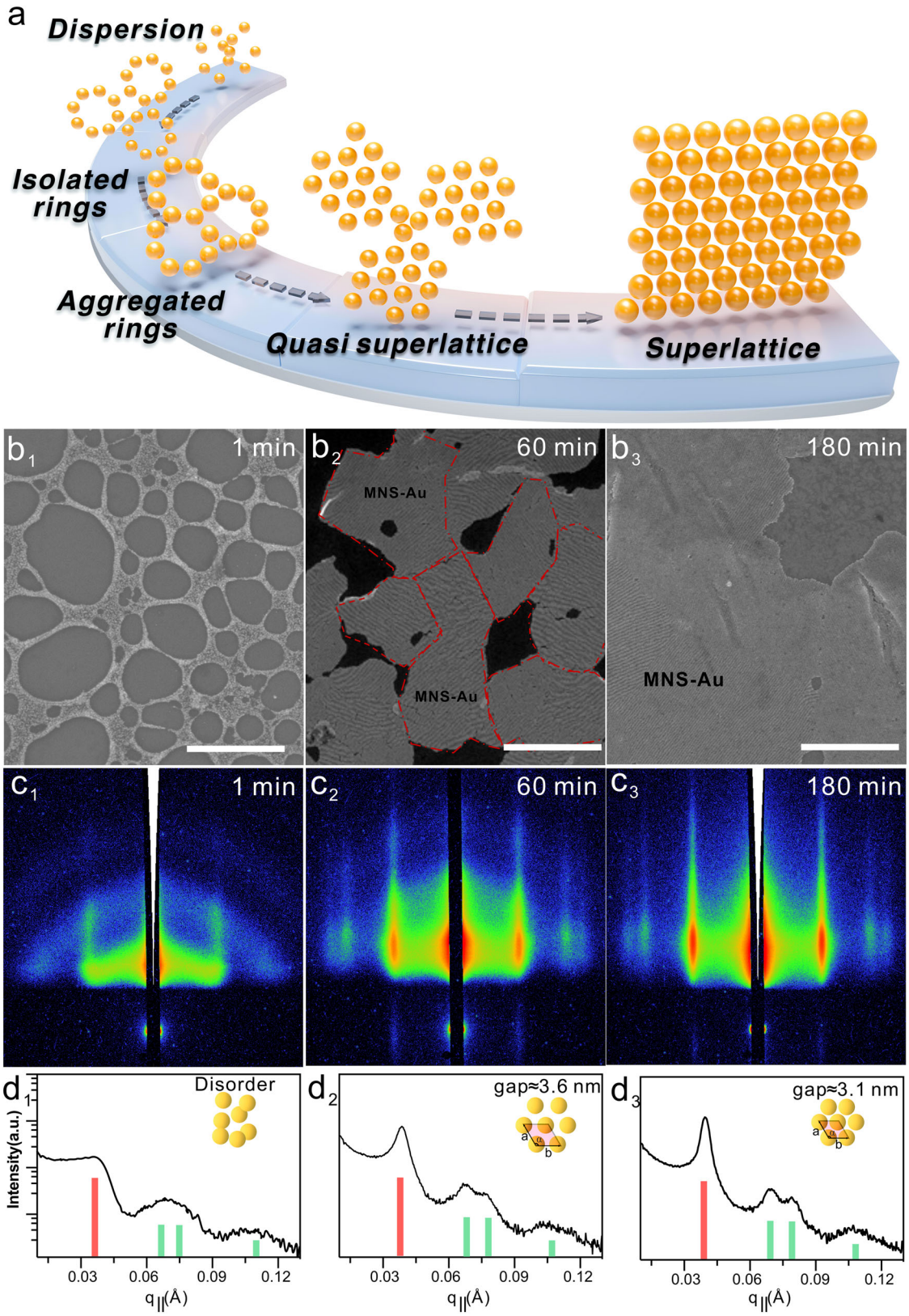

Fig. 1 | Characterization of the monolayer nanoparticle superlattice assembly and GISAXS and SEM measurements. a Illustration of the monolayer nanoparticle superlattice assembly. **b_1–b_3** SEM images of the dried AuNPs (~13 nm) on silicon substrates (all the scale bars are 1 μm), and the red dashed lines show the superlattices of different sheet types. High-magnification SEM image in the lower left corner at 180 min **b_3**; the scale bar is 100 nm. **c_1–c_3** GISAXS patterns recorded during the self-assembly of AuNPs at the air/DEG interface at 1, 60, and 180 min. **d_1–d_3** GISAXS 1D scattering profiles extracted from the corresponding GISAXS patterns, with schematic diagrams of the superlattice structures obtained from the theoretical calculation in the upper right corner; the crystal plane spacing is disordered, ~3.6 nm and ~3.1 nm.

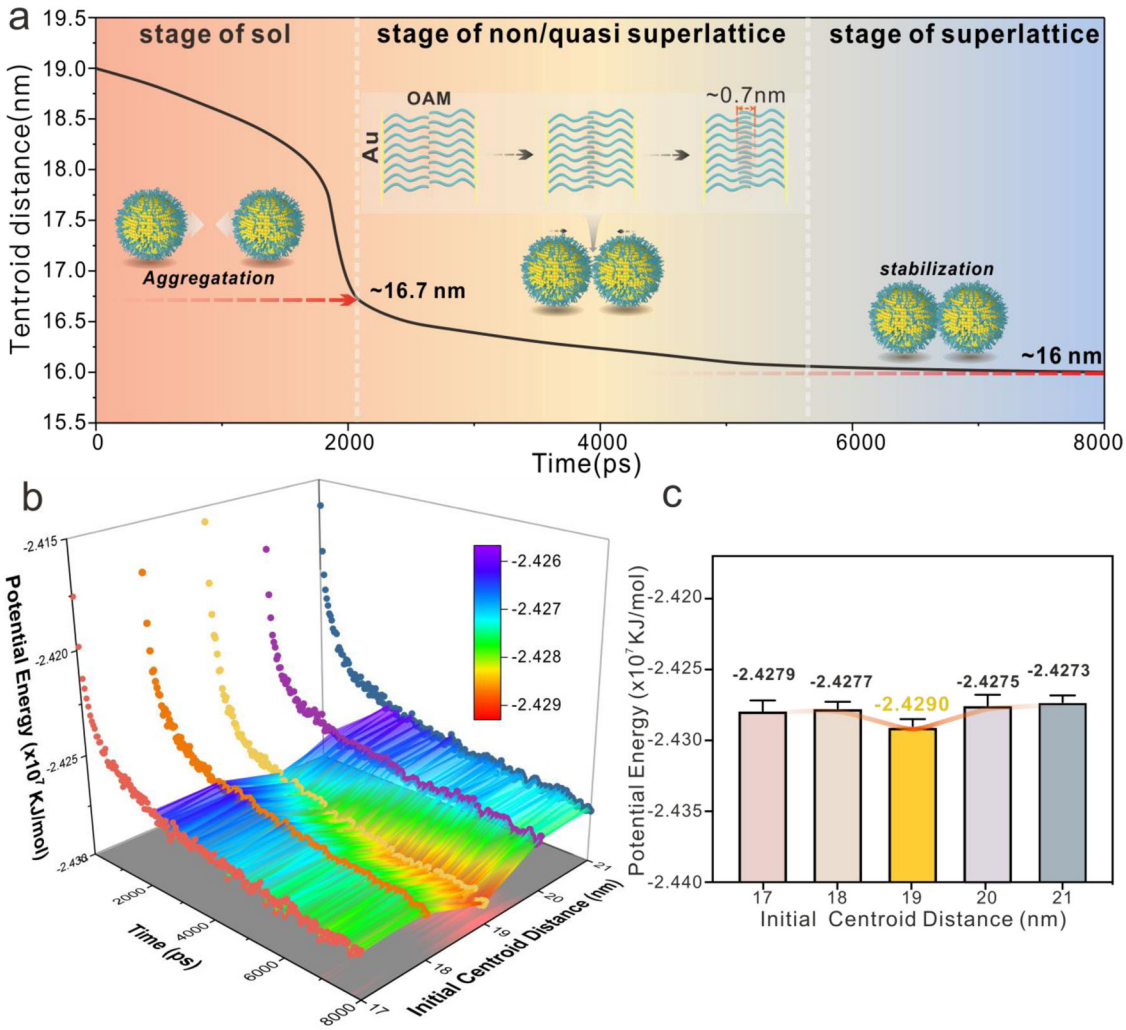

Fig. 2 | Calculated centroid distance and interparticle potential energy for AuNPs (~13 nm) as a function of time during the formation of the superlattice. **a** Calculated centroid distance for AuNPs with a diameter of ~13 nm as a function of time; the initial centroid distance was set to 19 nm. **b** Interparticle potential energy for AuNPs with a diameter of ~13 nm as a function of time for different initial centroid distances. The initial centroid distances set from the bottom to the top are 17 nm, 18 nm, 19 nm, 20 nm and 21 nm. **c** Final potential energy in the stability range (6000–8000 ps) and median boxplots for different initial centroid distances. The initial centroid distance ranges from 17 nm to 21 nm, the stable potential energy is divided into -2.4279×10^7 kJ/mol, -2.4277×10^7 kJ/mol, -2.4290×10^7 kJ/mol, -2.4275×10^7 kJ/mol, and -2.4273×10^7 kJ/mol, and there is a minimum at an initial distance of 19 nm (yellow column).

centroid distance and potential energy of AuNPs as a function of time to achieve a better explanation of the factors that influence the stability of superlattices. Figure 2a illustrates the time-dependent change in the centroid distance of ~13 nm AuNPs at an initial distance of 19 nm during the formation of the superlattice and the interplay of ligands. In this model, we employed GROMACS to separate the interparticle interactions into van der Waals interactions and Coulombic interactions. van der Waals interactions are short-range interactions, with the majority of the energy reflected in EVdw-SR, while the long-range part is accounted for by dispersion correction, i.e., EDisper.-corr. Coulombic interactions refer to electrostatic interactions and are long-range interactions[43]. This simulation process can be divided into three stages with respect to superlattice assembly. In the sol stage, AuNPs are driven closer to each other by the evaporation force of toluene. This is evident in the decreasing distance between the nanoparticle centers of mass, as shown in Fig. 2a, where the slope of the curve gradually increases. At the same time, the rapid increase in the potential energy (Fig. 2b) provides support for accelerated approach of the particles within 1700–2000 ps, primarily due to the influence of OAM-OAM and OAM-Au van der Waals potentials. When the center of mass distance is reduced to approximately 16.7 nm, the curve in Fig. 2a suddenly becomes flat, indicating that the nanoparticles are about to collide. This result may be attributed to the electrostatic repulsion generated by the intercrossing of the outer OAM molecules on the AuNPs, which partially hinders further approach. The depth of OAM intercrossing, as inferred from the schematic representation in Fig. 2a, is estimated to be approximately 0.7 nm during the stage of the non/quasisuperlattice. Thus, in the superlattice stage, the potential energy curve tends to be flat and stable at -2.429×10^7 kJ/mol (Fig. 2c). The curve of the centroid distance with respect to time finally stabilizes at approximately 16 nm, so the gap for 13 nm AuNPs is ~3 nm. This is almost consistent with the spacing calculated by GISAXS (~3.1 nm). In addition, we also considered the interparticle potential energy and centroid distance for AuNPs (~13 nm) as a function of time for different initial distances and calculated the median of the final stabilized potential energy, which can be seen in Fig. 2b. From 17 to 21 nm, the potential energy curves are all roughly stable after 4000 ps. According to the potential energy surface diagram in Fig. 2b, there is a region of maximum potential energy, which is reflected in the red area for an initial distance of 19 nm from 6000 to 8000 ps. Interestingly, when the initial distance exceeds 19 nm, the distance between

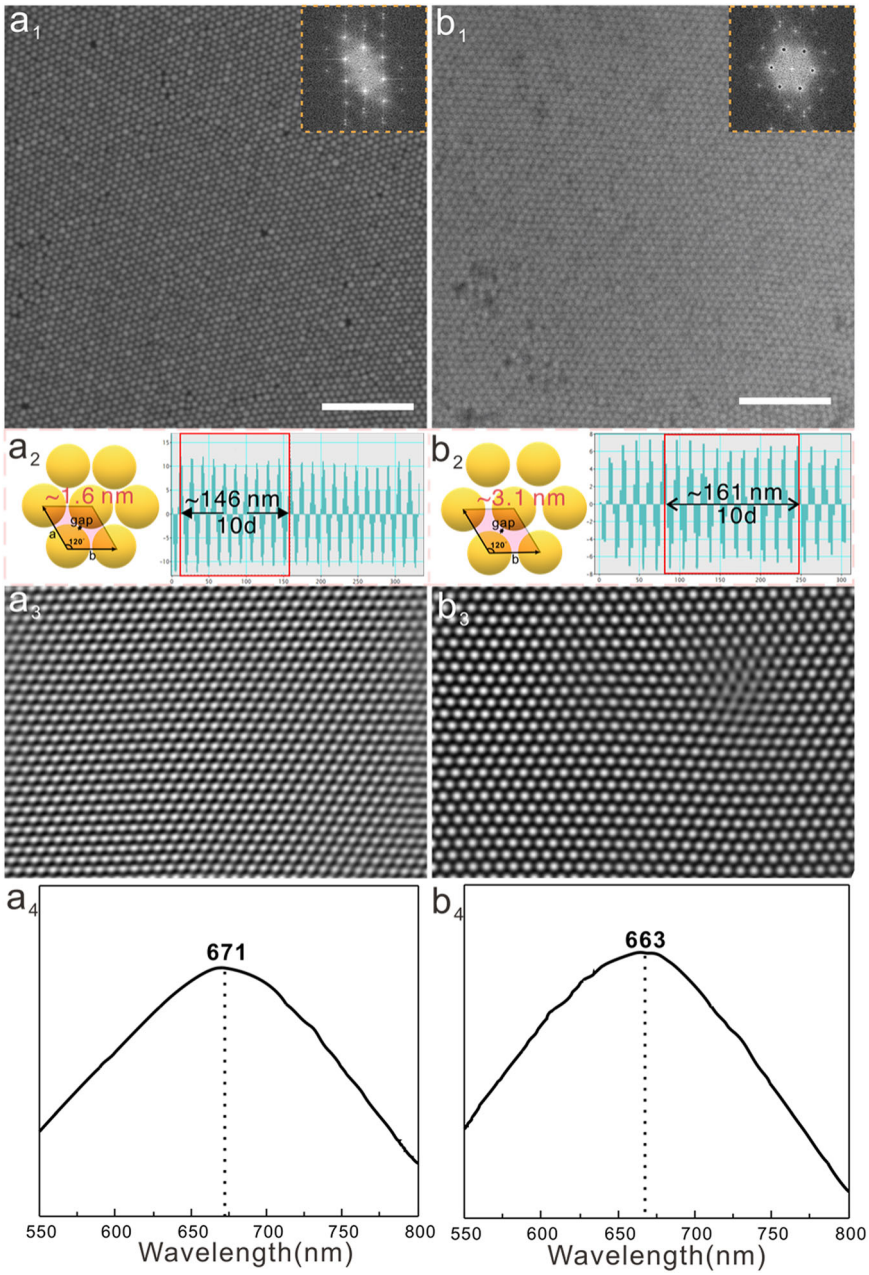

Fig. 3 | Characterization of optimized and normal AuNP (~13 nm) superlattices. $\mathbf{a_1}$, $\mathbf{b_1}$ SEM images of the optimized and normal monolayer Au nanoparticle superlattices (MSN-Au), the inset of which shows the Fourier pattern; the bars are 150 nm. $\mathbf{a_2}$, $\mathbf{b_2}$ Schematic diagrams (left) of the optimized and normal superlattice structures. The 10-plane spacings (10 d) are ~146 nm and ~161 nm, respectively, and the gaps of the optimized and normal structures are ~1.6 nm and ~3.1 nm, respectively. $\mathbf{a_3}$, $\mathbf{b_3}$ Inverse FFT images of MSN-Au with optimization and without optimization. $\mathbf{a_4}$, $\mathbf{b_4}$ PRRS for the optimized and normal superlattices.

AuNPs exceeds the range of their interaction potential, resulting in the nanoparticles undergoing free Brownian motion. As shown in Fig. 2c, a minimum value of -2.4290×10^7 kJ/mol is observed for an initial centroid distance of 19 nm (yellow bar), which indicates that the nanoparticle potential energy simulation is most stable under this condition. In contrast, when the initial distances are 20 and 21 nm, the distance between the centers of the nanoparticles continuously increases, which can be seen in Supplementary Fig. 6. Although the potential energy can remain stable after a certain period of motion, it is not the maximum van der Waals interaction potential. Therefore, considering the maximum potential energy and avoiding Brownian motion of nanoparticles, we chose an initial distance of 19 nm as the main analysis object. In summary, we determined that a distance between AuNPs of 16 nm exhibits the maximum total potential energy with an approximate gap of ~3 nm, indicating their optimal stability. This finding partially explains the tunability and stability of superlattice films, providing support for their diverse and homogeneous application in SERS.

Superlattice assembly for AuNPs of multiple sizes

To obtain the best SERS, we developed a rapid secondary film transfer method to adjust the interplanar spacing of the film and remove surface residues of DEG and OAM, thereby achieving the optimal state of the SERS substrate. Figure 3 shows the difference in the characteristics of optimized and normal AuNP (~13 nm) superlattices (the details of the experimental optimization method are shown in Supplementary Fig. 7 and this process is introduced in detail in Supplementary Note III).

Figure 3a_1, b_1 shows the permutation of the nanoparticles from optimized to normal, and through fast Fourier transform (FFT), hcp patterns can be obtained, indicating that this method does not destroy the structure of the superlattice. Then, we utilized the FFT pattern to obtain a schematic diagram of the superlattice, calculate the intercrystalline plane spacing, and further calculate the gaps between AuNPs (Fig. 3a_2, b_2). The gaps between AuNPs (~13 nm) before and after optimization are approximately 3.1 nm and 1.6 nm, respectively, and this trend of a decreased gap can also be proven by the inverse FFT (Fig. 3a_3, b_3). Additionally, the peak of plasmon

resonance Rayleigh scattering (PRRS) is at 663 nm, and with ethyl alcohol optimization, the maximum absorption peak redshifts to 671 nm (Fig. 3a_4, b_4), indicating a smaller gap, which is consistent with the data analysis of the gap calculation after FFT. Accordingly, this phenomenon may be due to the ethanol dissolving part of the OAM on the nanoparticle surface or changing its chain length[44,45], indicating that optimization has reduced the distance between hotspots and that DEG and OAM have been washed away, providing space for the entry of target molecules. This results in a great enhancement of the hotspot intensity per unit area, and the number of hotspots also increases. As shown in Supplementary Fig. 8, the electromagnetic field enhancement after optimization is 2 to 3 times that before optimization. Therefore, the optimized signal is significantly higher than the preoptimized signal for the 10^{-7} M CV SERS detection in Supplementary Fig. 9. Therefore, we prepared ordered and stable structures of small noble metal nanoparticles, generating numerous uniformly spaced hotspots, by using general superlattice assembly and further enhanced and purified the hotspots through optimization to improve the uniformity and reproducibility of detection. In addition, the details of the gap calculation of the optimized superlattice film for ~5 nm and ~7 nm AuNPs are shown in Supplementary Fig. 10, and the representations and SERS detection presented later are all the results of optimization.

After fabricating a monolayer nanoparticle superlattice, we demonstrated the generality of this method by assembling monolayer AuNP superlattices with different size nanoparticles. As shown in Fig. 4a_1, c_1, the resulting films for ~13 nm, ~7 nm and ~5 nm AuNPs (the UV absorption spectra for AuNPs of different sizes in the sol and superlattice states are shown in Supplementary Fig. 12 and material synthesis in detail in Supplementary Note IV). are all devoid of cracks and multilayers over an area of at least 4 μm^2, and they display Moiré patterns implying that the AuNPs self-assembled into an ordered array[37,46]. The insets in Fig. 4a_1, c_1 show the FFT patterns of the selected area in the SEM images, in which the points show a clear hexagonal-like array. Fig. 4a_2, c_2 shows the monolayer superlattices composed of AuNPs with diameters of ~13 nm, ~7 nm and ~5 nm under high magnification, exhibiting long-range periodicity and regularity. The insets in Fig. 4a_2, c_2 show transmission electron microscopy (TEM) images, and they further reveal hcp arrangements for different particle sizes, consistent with the positions of the GISAXS scattering peaks. Through image analysis, we determined the unit cell structures of the superlattices for the three different particle sizes, all of which possess a two-dimensional hexagonal superlattice structure. Specifically, a = b, and α = 120°. As shown in Fig. 4a_3, c_3, after optimization with the same ethanol concentration, the gap size increases with the nanoparticle diameter, and the ~13 nm, ~7 nm and ~5 nm nanoparticles (the particle distributions of AuNPs of different sizes are shown in Supplementary Fig. 11a–c) have superlattice gaps of ~1.6 nm, ~1.0 nm and ~0.9 nm, respectively. This may be due to the larger radius of curvature of the larger particles leading to more OAM molecules and more obvious interactions, which makes the long-range Coulomb interaction and repulsion stronger, leading to a shift of the potential well position to a large spacing[40,47]. In addition, Fig. 4a_4, c_4 shows that the thicknesses of the superlattice films composed of particles of different particle sizes are ~13 nm, ~7 nm and ~5 nm, which are similar to the diameters of a single particle, proving that the films are monolayers by AFM.

After the assembly of small particles into a superlattice and optimization, the detection limits for crystal violet (CV) are 10^{-8} M, 10^{-9} M and 10^{-10} M, as shown in Fig. 4a_5, c_5. Here, Considering the instability of SERS under low-concentration detection conditions, we adopts the characteristic peak probability detection method to determine the detection limit. Supplementary Fig. 13a–c shows the probability mapping of the SERS detection limit of different sizes of MSN-Au and the corresponding probability are all above 85%, ensuring the reliability of the detection limit. Compared with the SERS detection method with disorder films, the detection limit is decreased by 2–3 orders of magnitude with this monolayer superlattice (Supplementary Fig. 14). Additionally, as shown in Fig. 4a_6-c_6, the SERS intensities for CV at 1617 cm^{-1} show a relative standard deviation (RSD) of 9.01%, 9.51% and 14.86% across the whole region of 18 μm × 20 μm for ~13 nm, ~7 nm and ~5 nm AuNPs, respectively. We also compared studies on self-assembly or array assembly in SERS uniformity detection. Specifically, self-assembly mainly includes liquid-liquid[48,49], liquid-air[50,51], and drop-casting self-assembly[52]. These thin films on fixed substrates or silicon wafers exhibit a RSD of SERS for common probe molecules such as crystal violet (CV) and rhodamine (R6G) in the range of 5~13%. Therefore, compared with other studies, the SERS uniformity of superlattice films in our study shows a moderately low RSD, though it is not exceptionally low. The main reason for this phenomenon may be the inhomogeneity of the molecules on the superlattice surface caused by the method of drop-based detection. These results demonstrate that the as-prepared monolayer Au nanoparticle superlattices (MSN-Au) for different size NPs as SERS substrates can be used for the detection of analytes due to the high uniformity of their SERS signals. Notably, due to the high surface energy of ~5 nm particles, there may be partial multilayers in the spot field of view, resulting in signal enhancement.

Superlattice assembly for multiple categories of nanoparticles

In addition to the previously described superlattice assembly of small nanoparticles of different sizes, the method can be applied to different types of small nanoparticles (material synthesis in detail in Supplementary Note IV). After evaporation of the toluene phase, the interfacial self-assembly results in a large-area film with a homogeneous color across the entire surface of the DEG phase. Figure 5a_1, c_1 shows digital photos of monolayer Au nanoparticle superlattices (MSN-Au), monolayer Ag nanoparticle superlattices (MSN-Ag), and monolayer Au@Ag nanoparticle superlattices (MSN-Au@Ag) on DEG surfaces with an area of up to 20 cm^2, which show navy blue, magenta, and light violet colors, respectively, and 1 cm*1 cm monolayer films were successfully transferred through a silicon wafer (Supplementary Fig. 15a_2, c_2) and the particle distributions of the various types are shown in Supplementary Fig. 11a, d, e. The different colors are due to the differences in the absorption peaks of the various categories of nanoparticle superlattice films, and from the sol state to the superlattice, their absorption peaks all redshift closer to the excitation wavelength (633 nm), which can be seen in Supplementary Fig. 15. According to the energy-dispersive X-ray spectroscopy (EDS) analysis of the core-shell nanoparticles (Supplementary Fig. 16), both gold and silver are present. However, only the absorption peak of silver is observed in the UV absorption spectrum of the core-shell nanoparticle sol, indicating the synthesis of Au@Ag NPs. As shown in Fig. 5a_2, c_2, the resulting films for AuNPs, AgNPs and Au@Ag NPs also display Moiré patterns with an area of at least 4 μm^2 under low-magnification SEM imaging, and the FFT patterns of the SEM areas in the insets show a hexagonal-like array similar to the superlattices of multiple sizes. Furthermore, Fig. 5a_3, c_3 shows that the superlattices composed of AuNPs, AgNPs, and Au@Ag NPs also exhibit long-range periodicity and regularity under high magnification. The insets in Fig. 5a_3, c_3 show TEM images, and they further reveal hcp arrangements of the different types.

As shown in Fig. 5a_4, c_4, after the assembly of small particles into a superlattice and optimization, the CV detection limits of MSN-Au, MSN-Ag, and MSN-Au@Ag are 10^{-8} M, 10^{-9} M, and 10^{-11} M, respectively. Supplementary Fig. 13c–e shows the probability mapping of the SERS detection limit of different types of superlattice films and the corresponding probability are all above 90%. In addition, there is a charge transfer effect between the gold core and the silver shell of gold-silver core-shell particles, where electrons transfer from the gold core to the silver shell. This charge transfer enhances the SERS signal and improves the detection sensitivity. Therefore, MSN-Au@Ag is better than the other categories of nanoparticles in SERS detection. Compared with the SERS detection method with disorder films, the detection limit is decreased by 2–3 orders of magnitude with this monolayer superlattice (Supplementary Fig. 17), and its uniformity is improved. As shown in Fig. 5a_5, c_5, the RSD in the intensity of the CV characteristic peak at 1617 cm^{-1} is 9.01%, 15.90% and 14.37% across the whole region of 18 μm × 20 μm for MSN-Au, MSN-Ag, and MSN-Au@Ag, respectively.

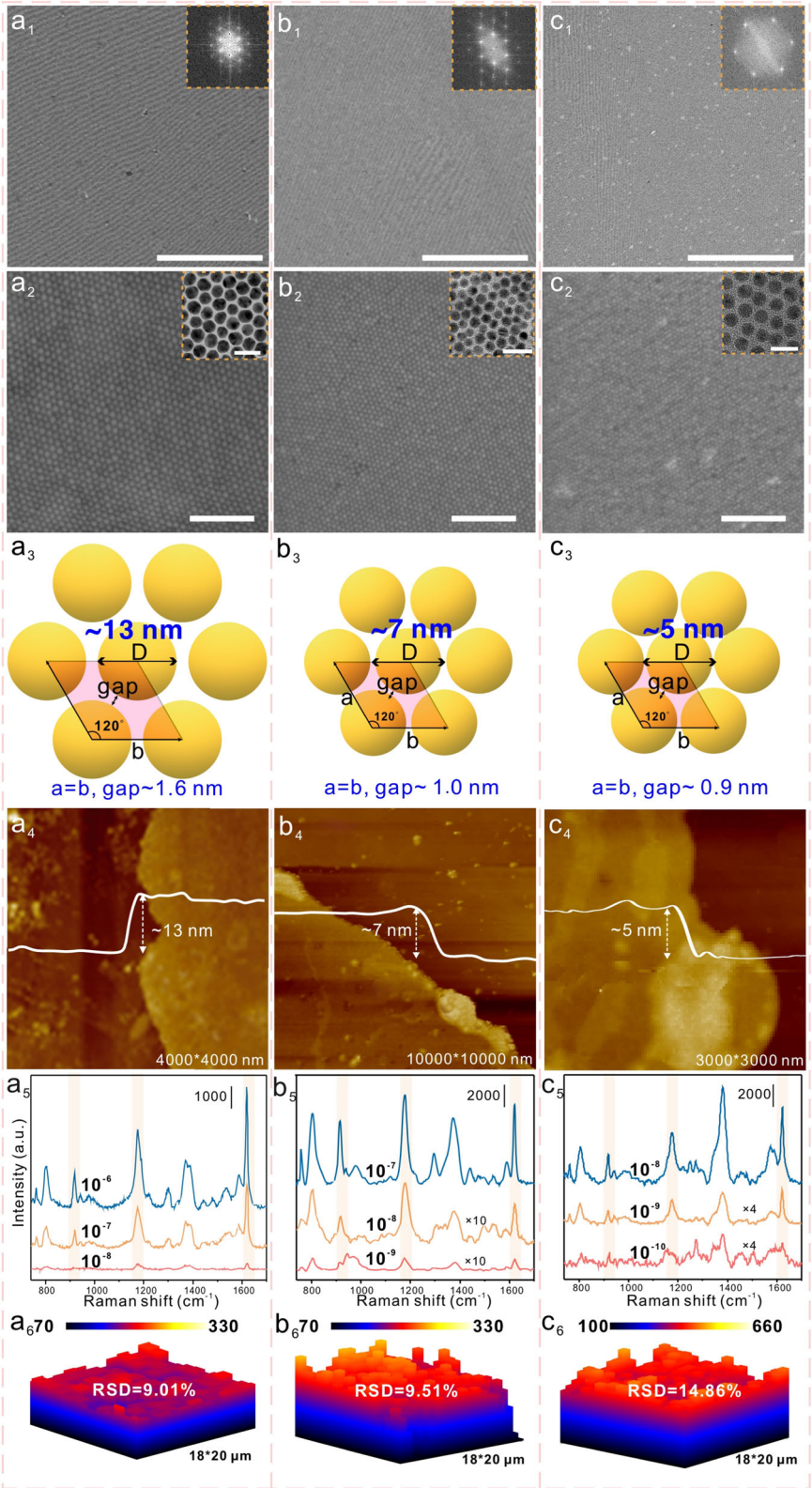

Fig. 4 | Characterization of monolayer superlattices for AuNPs of different sizes. **a_1, b_1, c_1** Low-magnification SEM images of the monolayer superlattices of ~13 nm, ~7 nm, and ~5 nm AuNPs (all the scale bars are 1 μm). Digital FFT patterns of a selected area are shown in the upper right corner, displaying the typical features of an hcp arrangement. **a_2, b_2, c_2** High-magnification SEM images of the monolayer superlattices of ~13 nm, ~7 nm, and ~5 nm AuNPs (all the scale bars are 200 nm) and TEM images in the upper right corner; the scale bars are 20 nm, 20 nm, and 10 nm, respectively. **a_3, b_3, c_3** Schematic diagrams of the superlattice structures of ~13 nm, ~7 nm, and ~5 nm AuNPs, which have gaps of ~1.6 nm, ~1.0 nm and ~0.9 nm, and all the superlattice films have been optimized. **a_4, b_4, c_4** AFM images and corresponding height profiles for AuNPs of different sizes. **a_5, b_5, c_5** SERS spectra for monolayer superlattices of ~13 nm, ~7 nm, and ~5 nm AuNPs for the detection of CV solutions with concentrations ranging from 10^{-6} to 10^{-8} M, 10^{-7} to 10^{-9} M, and 10^{-8} to 10^{-10} M, respectively. The wavelength and power of the laser were 633 nm and 1.94 mW, respectively, and the acquisition time was 5 s. Three pale yellow rectangles indicate the three main characteristic peaks of the CV, which are 913 cm^{-1},1172 cm^{-1}, and 1617 cm^{-1}. **a_6, b_6, c_6** 3D SERS mappings of the signal intensity of the peak at 1617 cm^{-1} for 10^{-7} M CV obtained from ~13 nm, ~7 nm and ~5 nm AuNPs. All maps are 20*18 μm in size with 360 points. The wavelength and power of the laser were 633 nm and 0.972 mW, respectively, and the acquisition time is 1 s.

Conclusions

We successfully designed a strategy for the self-assembly of noble metal nanoparticles less than 15 nm in size into monolayer superlattices, and the potential energy changes between the nanoparticles were studied using molecular dynamics simulations. Furthermore, this method is applicable to the assembly of small noble metal nanoparticles of various sizes (~5 nm, ~7 nm, ~13 nm) and types (Au, Ag, Au@Ag NPs), showcasing its generality. Compared to SERS detection of disorder films, the detection limit is reduced by 2 or 3 orders of magnitude for superlattices. Moreover, our study provides a new way to prepare SERS substrates with higher sensitivity, reproducibility, and uniformity by our rapid optimization method, and the minimum RSD is as low as ~9%. This general method provides a new

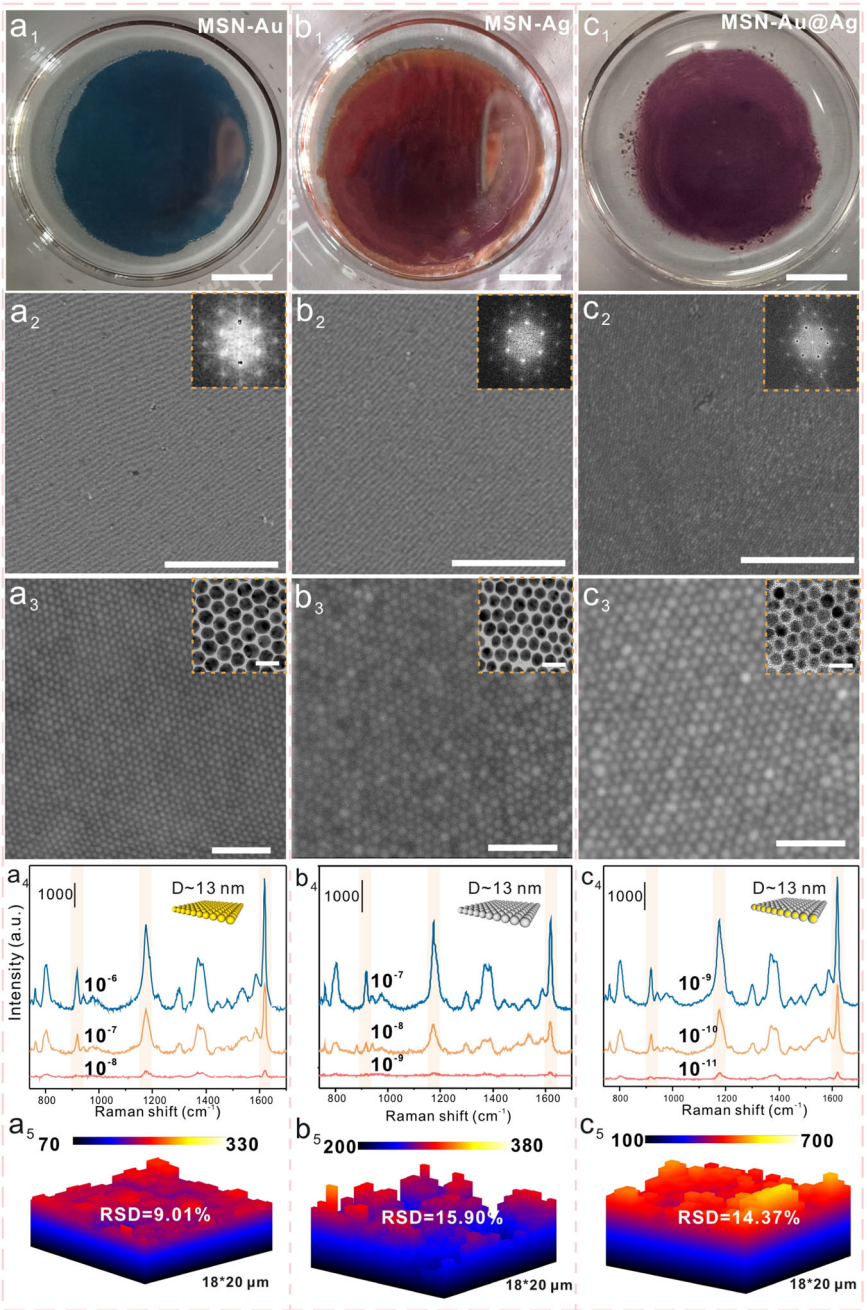

Fig. 5 | Characterization of monolayer superlattices for different noble metal nanoparticles (~13 nm). **a_1, b_1, c_1** Photos of the monolayer superlattices of AuNPs, AgNPs and Au@Ag NPs (all the scale bars are 1 cm). **a_2, b_2, c_2** Low-magnification SEM images of the monolayer superlattices of AuNPs, AgNPs and Au@Ag NPs (all the scale bars are 1 μm). Digital FFT patterns of a selected area are shown in the upper right corner, exhibiting the typical features of an hcp arrangement. **a_3, b_3, c_3** High-magnification SEM images of the monolayer superlattices of AuNPs, AgNPs and Au@Ag NPs (all the scale bars are 200 nm) and TEM images in the upper right corner (all the scale bars are 20 nm). **a_4, b_4, c_4** SERS spectra for the monolayer superlattices of AuNPs, AgNPs and Au@Ag NPs for the detection of CV solutions with concentrations ranging from 10^{-6} to 10^{-8} M, 10^{-7} to 10^{-9} M, and 10^{-8} to 10^{-11} M, respectively. The wavelength and power of the laser were 633 nm and 1.94 mW, respectively, and the acquisition time was 5 s. Three pale yellow rectangles indicate the three main characteristic peaks of the CV, which are 913 cm^{-1}, 1172 cm^{-1}, and 1617 cm^{-1}. **a_5, b_5, c_5** 3D SERS mappings of the signal intensity of the peak at 1617 cm^{-1} for 10^{-7} M CV obtained from AuNPs, AgNPs and Au@Ag NPs. All maps are 20*18 μm in size with 360 points. The wavelength and power of the laser were 633 nm and 0.972 mW, respectively, and the acquisition time is 1 s.

approach for highly sensitive and uniform SERS with all kinds of small nanoparticles.

Methods

Materials

Hydrogen tetrachloroaurate(III) tetrahydrate ($HAuCl_4 \cdot 4H2O$), Trisodium citrate dihydrate ($Na_3C_6H_5O_7 \cdot 2H_2O$, 99 %), ascorbic acid (AA, 99.7%), ammonia water ($NH3 \cdot H2O$, 25% ~ 28%), toluene (C_7H_8), and ethanol absolute (C_2H_6O, 99.7 %), crystal violet ($C_{25}H_{30}N_3Cl$), Silver nitrate ($AgNO_3$, 99.995%), were purchased from Sinopharm Chemical Reagent Co. Ltd. potassium carbonate (≥99%) and tannic acid (MW 1701, ACS reagent) were purchased from Sigma-Aldrich. Oleylamine ($C_{18}H_{37}N$) and diethylene glycol ($C_4H_{10}O_3$, 98 %) were purchased from Aladdin Industrial Co. Ltd and Shanghai Titan Scientific Co. Ltd, respectively. chemicals were used as received without further purification. The Milli-Q water was used in all experiments (18.25 MΩcm, Millipore).

Synthesis of Au nanoparticles for ~5 nm

The Au sols were synthesized following the method of (citation). Basically, a reducing solution of sodium citrate (SC, 2.2 mM) with 0.1 mL of tannic acid (TA, 2.5 mM) and 1 mL of potassium carbonate (K_2CO_3, 150 mM) was heated in a 250 mL three-necked round-bottom flask with a heating mantle and stirred vigorously. When the temperature reached 70 °C, 1 mL of tetra chloroauric acid ($HAuCl_3$, 25 mM) was added[53].

Synthesis of Au nanoparticles for ~7 nm and ~13 nm

The ~5 nm Au NPs were prepared using the same protocol as above. Right after the synthesis and without changing the reaction vessel, the sample was diluted by taking out 55 mL and adding 55 mL of SC (2.2 mM). When the temperature reached 70 °C again, two doses of 0.5 mL of $HAuCl_4$ (25 mM) were added with a 10 min gap between them. This growth step of sample dilution and 2 doses of $HAuCl_4$ was repeated until the particles reached ~7 nm and ~13 nm. Detailed methods are given in Victor Puntes[53].

Synthesis of Ag nanoparticles for ~13 nm

The aqueous synthesis of Ag NPs is based on a reported improved seeded-growth strategy. A similar growth strategy for Au nanoparticles was employed to produce ~13 nm Ag particles stabilized by sodium citrate[54].

Synthesis of Au@Ag NPs for ~13 nm

The following method was used to synthesize Au NPs with an average size of 7 nm. The preparation process of Au@Ag NPs was as follows[55]: First, a silver–ammonia complex solution was obtained by mixing 1 mL of $AgNO_3$ solution (10 mM) with 0.17 mL of ammonia water (25–28%). Next, 200 μL of the AuNP seed solution with an average size of 5.5 nm was added to the solution.

Synthesis of OAM-Au/Ag/Au@Ag NPs for ~13 nm

The OAM-AuNPs were prepared by using the conventional phase transfer technology method reported in the literature and this method is also suitable for other kinds of nanoparticles[40]. Specifically, the citrate-stabilized AuNPs prepared above were dispersed into the toluene phase (OAM, 1 mM) by shaking vigorously. Then, the OAM-AuNPs in the toluene phase were collected for further use.

Apparatus

An inverted microscope (eclipse Ti−U, Nikon, Japan) equipped with a dark-field condenser (0.8 < NA < 0.95) and a 40× objective lens (NA = 0.8) was used.(USTC, He Fei), for the real-time monitoring of the forming of superlattice film. Raman spectra were performed on a Lab-RAM HR800 spectrometer with a 633 nm laser excitation source. The instrument model used for grazing-incidence small-angle X-ray scattering (GISAXS) testing is Xeuss 2.0, which from xenos Inc, France.

SERS measurements

In this study, all superlattice SERS substrates underwent optimization (regulating the gap with ethanol solution) prior to their detection. For the sensitivity detection of SERS, 5 μl of ethanol solution containing the target was dropped onto the surface of the superlattice substrate, and SERS spectral signals were immediately collected until the solvent completely evaporated. The entire process lasted for 1–1.5 min, with focus maintained throughout. For the detection of SERS uniformity, 5 μl of ethanol solution containing the target material was dropped onto the surface of the superlattice substrate. After waiting for 2–3 min for the solvent to evaporate completely, the collection of SERS mapping was initiated. For the sensitivity detection of SERS, a laser with a wavelength of 633 nm and a power of 1.94 mW was employed, utilizing a magnification of ×50 and an accumulation time of 5 s. For the detection of SERS uniformity, a laser with a wavelength of 633 nm and a power of 0.92 mW was used, along with a magnification of ×50 and an accumulation time of 1 s.

Grazing-incidence small-angle X-ray scattering (GISAXS) measurements

GISAXS is a special technique widely used to measure the scattering of nanosized objects at surfaces. The scattering vector q is the difference between the incoming and outgoing wavevectors, $q \equiv k_f - k_i$, which in the case of cylinder symmetry is most conveniently decomposed into in-plane and out-of-plane components $q_{||}$ and q_z. The ordinate of the data is the intensity I, and the abscissa is the scattering vector q ($Å^{-1}$), which can be converted into 2θ coordinates by the formula: $q = \frac{4\pi \sin\theta}{\lambda}$. Since GISAXS measurements are carried out in the small-angle regime, Lorentz and polarization corrections are negligible. The experimental conditions for GISAXS measurements made at silicon wafer include the following: Sample detector distance(SDD) is 2480 mm, The phototube power of the copper target was 30 W, the wavelength was 1.54189 Å, the detector used was Pilatus 3 R 300 K, and the single pixel size was 172 μm. The experiment was conducted at the University of Science and Technology of China.

Dark-field measurements

Dark-field measurements were conducted using an inverted microscope (eclipse Ti-U, Nikon, Japan) equipped with a dark-field condenser (0.8 < NA < 0.95) and a 40x objective lens (NA = 0.8). A 100-W halogen lamp provided white light to excite the NPs and generate plasmon resonance scattering light. The dark-field color images were acquired using a true-color digital camera (Nikon DS-fi).

SEM measurements

SEM measurements The scanning electron microscopy (SEM) images were taken by an Auriga focused ion-beam scanning electron microscopy (FIB-SEM), equipped with X-ray energy dispersive spectroscopy (EDS) capabilities, operated at an acceleration voltage of 15 kV.

UV–Vis absorption spectrum measurements

Ultraviolet–visible (UV–vis) spectrum were performed on a VIS miniature optical fiber spectrometer (Insion, Germany), corrected against the background spectrum, and normalized to zero absorbance at 800 nm.

Electromagnetic simulations

The electromagnetic simulations were carried out by the finite-element method based on the commercial software of COMSOL Multiphysics. Periodic conditions were employed to simulate the AuNPs superlattice. The permittivity for Au, Si, SiO_2 were taken from refs. 56–58, respectively. Oleylamine was treated as a thin layer wraps the particle films was refractive index of 1.46. The transmittance T was obtained directly through port and absorbance was calculated through $\mathbf{lg(1/T)}$.

Data availability

The data that support the findings of this study are presented in the manuscript and supplementary information file. Source data are available from the corresponding author upon request.

Received: 20 October 2023; Accepted: 16 April 2024;
Published online: 30 April 2024

References

1. Fleischmann, M., Hendra, P. J. & McQuillan, A. J. Raman spectra of pyridine adsorbed at a silver electrode. *Chem. Phys. Lett.* **26**, 163–166 (1974).
2. Jeanmaire, D. L. & Van Duyne, R. P. Surface raman spectroelectrochemistry: Part I. Heterocyclic, aromatic, and aliphatic amines adsorbed on the anodized silver electrode. *J. Electroanalytical Chem. Interfacial Electrochem.* **84**, 1–20 (1977).
3. Langer, J. et al. Present and Future of Surface-Enhanced Raman Scattering. *ACS Nano* **14**, 28–117 (2020).
4. Nie, S. & Emory, S. R. Probing Single Molecules and Single Nanoparticles by Surface-Enhanced Raman Scattering. *Science* **275**, 1102–1106 (1997).
5. Su, X. et al. Integrated SERS-Vertical Flow Biosensor Enabling Multiplexed Quantitative Profiling of Serological Exosomal Proteins in Patients for Accurate Breast Cancer Subtyping. *ACS Nano* **17**, 4077–4088 (2023).
6. Ramos, R. M. C. R. et al. Hyperbranched Au Nanocorals for SERS Detection of Dye Pollutants. *ACS Appl. Nano Mater.* **6**, 3963–3973 (2023).
7. Martinez, L. & He, L. Detection of Mycotoxins in Food Using Surface-Enhanced Raman Spectroscopy: A Review. *ACS Appl. Bio Mater.* **4**, 295–310 (2021).
8. Liu, W. et al. Utilizing an Automated SERS-Digital Microfluidic System for High-Throughput Detection of Explosives. *ACS Sens.* **8**, 1733–1741 (2023).
9. Chen, C. et al. High spatial resolution nanoslit SERS for single-molecule nucleobase sensing. *Nat. Commun.* **9**, 1733 (2018).

10. Kleinman, S. L. et al. Single-Molecule Surface-Enhanced Raman Spectroscopy of Crystal Violet Isotopologues: Theory and Experiment. *J. Am. Chem. Soc.* **133**, 4115–4122 (2011).
11. Ge, M. et al. General Surface-Enhanced Raman Spectroscopy Method for Actively Capturing Target Molecules in Small Gaps. *J. Am. Chem. Soc.* **143**, 7769–7776 (2021).
12. Zargartalebi, H., Hejazi, S. H. & Sanati-Nezhad, A. Self-assembly of highly ordered micro- and nanoparticle deposits. *Nat. Commun.* **13**, 3085 (2022).
13. Wu, L.-A., Li, W.-E., Lin, D.-Z. & Chen, Y.-F. Three-Dimensional SERS Substrates Formed with Plasmonic Core-Satellite Nanostructures. *Sci. Rep.* **7**, 13066 (2017).
14. Zhang, L. et al. Quantitative Detection of Creatinine in Human Serum by SERS with Evaporation-Induced Optimal Hotspots on Au Nanocubes. *ACS Appl. Nano Mater.* **5**, 4841–4847 (2022).
15. Liu, J.-W. et al. Ordering Ag nanowire arrays by a glass capillary: A portable, reusable and durable SERS substrate. *Sci. Rep.* **2**, 987 (2012).
16. Camden, J. P. et al. Probing the Structure of Single-Molecule Surface-Enhanced Raman Scattering Hot Spots. *J. Am. Chem. Soc.* **130**, 12616–12617 (2008).
17. Le Ru, E. C., Blackie, E., Meyer, M. & Etchegoin, P. G. Surface Enhanced Raman Scattering Enhancement Factors: A Comprehensive Study. *J. Phys. Chem. C.* **111**, 13794–13803 (2007).
18. Kleinman, S. L., Frontiera, R. R., Henry, A.-I., Dieringer, J. A. & Van Duyne, R. P. Creating, characterizing, and controlling chemistry with SERS hot spots. *Phys. Chem. Chem. Phys.* **15**, 21–36 (2013).
19. Bell, S. E. J. & Sirimuthu, N. M. S. Quantitative surface-enhanced Raman spectroscopy. *Chem. Soc. Rev.* **37**, 1012–1024, (2008).
20. Cialla, D. et al. Surface-enhanced Raman spectroscopy (SERS): progress and trends. *Anal. Bioanal. Chem.* **403**, 27–54 (2012).
21. Ding, S.-Y., You, E.-M., Tian, Z.-Q. & Moskovits, M. Electromagnetic theories of surface-enhanced Raman spectroscopy. *Chem. Soc. Rev.* **46**, 4042–4076 (2017).
22. Willets, K. A. & Van Duyne, R. P. Localized surface plasmon resonance spectroscopy and sensing. *Annu. Rev. Phys. Chem.* **58**, 267–297 (2007).
23. Emory, S. R. & Nie, S. Screening and enrichment of metal nanoparticles with novel optical properties. *J. Phys. Chem. B* **102**, 493–497 (1998).
24. Zeman, E. J. & Schatz, G. C. AN ACCURATE ELECTROMAGNETIC THEORY STUDY OF SURFACE ENHANCEMENT FACTORS FOR AG, AU, CU, LI, NA, AL, GA, IN, ZN, AND CD. *J. Phys. Chem.* **91**, 634–643 (1987).
25. Benz, F. et al. SERS of Individual Nanoparticles on a Mirror: Size Does Matter, but so Does Shape. *J. Phys. Chem. Lett.* **7**, 2264–2269 (2016).
26. Perovic, M., Tarakina, N. V., Hofmann, J. P. & Oschatz, M. Influence of Local Environments in Pores of Different Size on the Catalytic Liquid-Phase Oxidation of d-Glucose by Au Nanoparticles Supported on Nanoporous Carbon. *ACS Appl. Nano Mater.* **3**, 7695–7703 (2020).
27. Veisi, H., Abassi, P., Mohammadi, P., Tamoradi, T. & Karmakar, B. Gold nanoparticles decorated biguanidine modified mesoporous silica KIT-5 as recoverable heterogeneous catalyst for the reductive degradation of environmental contaminants. *Sci. Rep.* **11**, 2734 (2021).
28. Kotov, N. A., Meldrum, F. C., Wu, C. & Fendler, J. H. monoparticulate layer and langmuir-blodgett-type multiparticulate layers of size-quantized cadmium-sulfide clusters - a colloid-chemical approach to superlattice construction. *J. Phys. Chem.* **98**, 2735–2738 (1994).
29. Shani, L. et al. DNA-assembled superconducting 3D nanoscale architectures. *Nat. Commun.* **11**, 5697 (2020).
30. Yan, N., Liu, X., Zhu, J., Zhu, Y. & Jiang, W. Well-Ordered Inorganic Nanoparticle Arrays Directed by Block Copolymer Nanosheets. *ACS Nano* **13**, 6638–6646 (2019).
31. Lu, X. et al. Light-Controlled Shrinkage of Large-Area Gold Nanoparticle Monolayer Film for Tunable SERS Activity. *Chem. Mater.* **30**, 1989–1997 (2018).
32. Zhong, Y., Allen, V. R., Chen, J., Wang, Y. & Ye, X. Multistep Crystallization of Dynamic Nanoparticle Superlattices in Nonaqueous Solutions. *J. Am. Chem. Soc.* **144**, 14915–14922 (2022).
33. Kalsin, A. M. et al. Electrostatic Self-Assembly of Binary Nanoparticle Crystals with a Diamond-Like Lattice. *Science* **312**, 420–424 (2006).
34. Dong, A., Chen, J., Vora, P. M., Kikkawa, J. M. & Murray, C. B. Binary nanocrystal superlattice membranes self-assembled at the liquid-air interface. *Nature* **466**, 474–477 (2010).
35. Zhang, M. et al. Core–Shell and Asymmetric Polystyrene–Gold Composite Particles via One-Step Pickering Emulsion Polymerization. *Langmuir* **30**, 75–82 (2014).
36. Xiao, Y. et al. Generation of Fermat's spiral patterns by solutal Marangoni-driven coiling in an aqueous two-phase system. *Nat. Commun.* **13**, 7206 (2022).
37. Hattori, T., Kawamura, N., Iimori, T., Miyamachi, T. & Komori, F. Subatomic Distortion of Surface Monolayer Lattice Visualized by Moiré Pattern. *Nano Lett.* **21**, 2406–2411 (2021).
38. Schultz, S., Smith, D. R., Mock, J. J. & Schultz, D. A. Single-target molecule detection with nonbleaching multicolor optical immunolabels. *Proc. Natl Acad. Sci.* **97**, 996–1001 (2000).
39. Faulds, K., Littleford, R. E., Graham, D., Dent, G. & Smith, W. E. Comparison of surface-enhanced resonance Raman scattering from unaggregated and aggregated nanoparticles. *Anal. Chem.* **76**, 592–598 (2004).
40. Hassinen, J., Liljeström, V., Kostiainen, M. A. & Ras, R. H. A. Rapid Cationization of Gold Nanoparticles by Two-Step Phase Transfer. *Angew. Chem. Int. Ed.* **54**, 7990–7993 (2015).
41. Wu, L., Wang, X., Wang, G. & Chen, G. In situ X-ray scattering observation of two-dimensional interfacial colloidal crystallization. *Nat. Commun.* **9**, 1335 (2018).
42. Lu, B. et al. Tunable Subnanometer Gaps in Self-Assembled Monolayer Gold Nanoparticle Superlattices Enabling Strong Plasmonic Field Confinement. *ACS Nano* **17**, 12774–12787 (2023).
43. Ambrosetti, A., Ferri, N., DiStasio, R. A. & Tkatchenko, A. Wavelike charge density fluctuations and van der Waals interactions at the nanoscale. *Science* **351**, 1171–1176 (2016).
44. Von White, G. II, Mohammed, F. S. & Kitchens, C. L. Small-Angle Neutron Scattering Investigation of Gold Nanoparticle Clustering and Ligand Structure Under Antisolvent Conditions. *J. Phys. Chem. C.* **115**, 18397–18405 (2011).
45. Pei, L., Mori, K. & Adachi, M. Investigation on arrangement and fusion behaviors of gold nanoparticles at the air/water interface. *Colloids Surf. A.* **281**, 44–50 (2006).
46. Singh, A., Dickinson, C. & Ryan, K. M. Insight into the 3D Architecture and Quasicrystal Symmetry of Multilayer Nanorod Assemblies from Moiré Interference Patterns. *ACS Nano* **6**, 3339–3345 (2012).
47. Xing, L., Wang, C., Cao, Y., Zhang, J. & Xia, H. Macroscopical monolayer films of ordered arrays of gold nanoparticles as SERS substrates for in situ quantitative detection in aqueous solutions. *Nanoscale* **13**, 14925–14934 (2021).
48. Li, S., Liu, L. & Hu, J. An approach for fabricating self-assembled monolayer of gold nanoparticles on NH2⁺ ion implantation modified indium tin oxide as the SERS-active substrate. *Spectrochim. Acta Part A Mol. Biomolecular Spectrosc.* **86**, 533–537 (2012).
49. Tang, S. et al. Efficient Enrichment and Self-Assembly of Hybrid Nanoparticles into Removable and Magnetic SERS Substrates for Sensitive Detection of Environmental Pollutants. *Acs Appl. Mater. Interfaces* **9**, 7472–7480 (2017).
50. Guo, Q., Xu, M., Yuan, Y., Gu, R. & Yao, J. Self-Assembled Large-Scale Monolayer of Au Nanoparticles at the Air/Water Interface Used as a SERS Substrate. *Langmuir* **32**, 4530–4537 (2016).
51. Chen, X. et al. Slippery Au Nanosphere Monolayers with Analyte Enrichment and SERS Enhancement Functions. *Nano Lett.* **23**, 6736–6743 (2023).

52. Zhang, L. et al. Highly active Au NP microarray films for direct SERS detection. *J. Mater. Chem. C.* **7**, 15259–15268 (2019).
53. Piella, J., Bastús, N. G. & Puntes, V. Size-Controlled Synthesis of Sub-10-nanometer Citrate-Stabilized Gold Nanoparticles and Related Optical Properties. *Chem. Mater.* **28**, 1066–1075 (2016).
54. Bastús, N. G., Piella, J. & Puntes, V. Quantifying the Sensitivity of Multipolar (Dipolar, Quadrupolar, and Octapolar) Surface Plasmon Resonances in Silver Nanoparticles: The Effect of Size, Composition, and Surface Coating. *Langmuir* **32**, 290–300 (2016).
55. Xing, L. X. et al. Large-Area Monolayer Films of Hexagonal Close-Packed Au@Ag Nanoparticles as Substrates for SERS-Based Quantitative Determination. *ACS Appl. Mater. Interfaces* **14**, 13480–13489 (2022).
56. Johnson, P. B. & Christy, R. W. Optical Constants of the Noble Metals. *Phys. Rev. B* **6**, 4370–4379 (1972).
57. Green, M. A. Self-consistent optical parameters of intrinsic silicon at 300K including temperature coefficients. *Sol. Energy Mater. Sol. Cells* **92**, 1305–1310 (2008).
58. Malitson, I. H. Interspecimen Comparison of the Refractive Index of Fused Silica. *J. Opt. Soc. Am.* **55**, 1205–1208 (1965).

Acknowledgements

This work was supported by the National Natural Science Foundation of China (52232007) and Hefei Key Generic Technology Research and Development Project (GJ2022GX20). The authors are profoundly grateful to the agencies that provided these grants.

Author contributions

L.B.Y. and C.Y. conceived and designed the experiments. C.Y. performed the theoretical calculations. C.Y. and W.W.Y. performed material synthesis, structural characterization and Raman measurements. L.B.Y. and C.Y. analyzed the data. C.Y. wrote the paper. R.L.D. and S.B.D. provided the instruments for testing.

Competing interests

The authors declare no competing interests.

Additional information

Supplementary information The online version contains supplementary material available at https://doi.org/10.1038/s43246-024-00506-3.

Correspondence and requests for materials should be addressed to Liangbao Yang.

Peer review information *Communications Materials* thanks the anonymous reviewers for their contribution to the peer review of this work. Primary Handling Editors: Jet-Sing Lee.

Reprints and permissions information is available at http://www.nature.com/reprints

Publisher's note Springer Nature remains neutral with regard to jurisdictional claims in published maps and institutional affiliations.

Open Access This article is licensed under a Creative Commons Attribution 4.0 International License, which permits use, sharing, adaptation, distribution and reproduction in any medium or format, as long as you give appropriate credit to the original author(s) and the source, provide a link to the Creative Commons licence, and indicate if changes were made. The images or other third party material in this article are included in the article's Creative Commons licence, unless indicated otherwise in a credit line to the material. If material is not included in the article's Creative Commons licence and your intended use is not permitted by statutory regulation or exceeds the permitted use, you will need to obtain permission directly from the copyright holder. To view a copy of this licence, visit http://creativecommons.org/licenses/by/4.0/.

© The Author(s) 2024